AGU ADVANCING EARTH AND SPACE SCIENCES

Earth and Space Science

RESEARCH ARTICLE
10.1029/2025EA004382

Identifying Wet Troposphere Delay in L-Band InSAR Using Weather Radar Reflectivity

Talib Oliver-Cabrera[1], **Cathleen E. Jones**[1], **Marc Simard**[1], **Bhuvan Varugu**[1,2], and **Saoussen Belhadj-Aissa**[1]

[1]Jet Propulsion Laboratory, California Institute of Technology, Pasadena, CA, USA, [2]Now at: California Department of Water Resources, Sacramento, CA, USA

Key Points:

- We identify wet troposphere interferometric phase delay on L-band measurements using a weather phase delay recognition algorithm
- We explore wet tropospheric delay impact magnitude on L-band interferometry
- High sampling rate weather radar can be used to identify rapidly changing wet troposphere in cases where existing models are insufficient

Supporting Information:

Supporting Information may be found in the online version of this article.

Correspondence to:

T. Oliver-Cabrera,
talib.oliver.cabrera@jpl.nasa.gov

Citation:

Oliver-Cabrera, T., Jones, C. E., Simard, M., Varugu, B., & Belhadj-Aissa, S. (2025). Identifying wet troposphere delay in L-band InSAR using weather radar reflectivity. *Earth and Space Science*, *12*, e2025EA004382. https://doi.org/10.1029/2025EA004382

Received 30 MAR 2025
Accepted 24 JUN 2025

Author Contributions:

Conceptualization: Talib Oliver-Cabrera, Cathleen E. Jones, Marc Simard
Data curation: Talib Oliver-Cabrera, Cathleen E. Jones, Bhuvan Varugu, Saoussen Belhadj-Aissa
Formal analysis: Talib Oliver-Cabrera, Bhuvan Varugu, Saoussen Belhadj-Aissa
Investigation: Talib Oliver-Cabrera, Cathleen E. Jones
Methodology: Talib Oliver-Cabrera, Cathleen E. Jones, Marc Simard

Abstract Synthetic Aperture Radar (SAR) pulses undergo variable propagation delays in the atmosphere due to changes in pressure, temperature, and humidity within the troposphere, causing large error in Interferometric SAR (InSAR) measurements of land surface displacement. Wet troposphere delay, resulting from condensed water and water vapor clouds, can introduce delays of tens of centimeters that significantly impact surface displacement estimates. This study provides unequivocal evidence of the wet troposphere's impact on InSAR phase measurements by examining spatial patterns in NOAA NEXRAD weather radar reflectivity and interferometric phase outliers. We utilize a feature-comparison approach with reflectivity data from NEXRAD radar stations to identify artifacts from wet tropospheric delays in InSAR phase measurements derived from rapid repeat-pass data acquired by UAVSAR L-band SAR. NEXRAD's 5-min scanning interval, compared to UAVSAR's 30-min revisit time, enabled detection of phase artifacts caused by fast-moving and developing clouds. We identify regions in InSAR interferograms with troposphere-induced phase artifacts by matching features common to InSAR phase outlier masks and NEXRAD high reflectivity masks. Matched results between InSAR phase noise and NEXRAD reflectivity show phase delays of up to 25 radians in L-band, corresponding to 48 cm of delay. Comparison with tropospheric delays calculated using the Generic Atmospheric Correction Online Service for InSAR (GACOS) showed global weather models lack sufficient spatial and temporal resolution to accurately estimate observed wet troposphere delays. While our study focused on UAVSAR, findings apply to other SAR missions, including L-band NISAR and ALOS2/4, aiding identification and interpretation of InSAR results affected by tropospheric delays.

Plain Language Summary In this study, we investigated how changes in the lowest layer of the Earth's atmosphere affect Interferometric Synthetic Aperture Radar (InSAR) measurements, particularly those caused by condensed water and water vapor clouds also known as wet troposphere delay. This delay occurs when water vapor and clouds in the troposphere alter the path of SAR pulses, leading to inaccuracies in surface displacement estimates. This study confirms the impact of wet troposphere delay on InSAR data by comparing weather radar data from NOAA NEXRAD stations to detect wet tropospheric delays in InSAR measurements obtained from UAVSAR. By comparing features in the radar data, we were able to pinpoint regions in the InSAR images where tropospheric delays were present. Our analysis revealed significant delays of up to 48 cm. While our study focused on UAVSAR, our findings are relevant for other SAR missions, like the upcoming NISAR mission, helping to improve the interpretation of SAR data affected by atmospheric delays.

1. Introduction

Interferometric synthetic aperture radar (InSAR) is a remote sensing technique used to measure spatially-extensive surface displacement with accuracies as good as a few millimeters (Bamler & Hartl, 1998; González, 2024). InSAR is commonly used to observe a wide range of phenomena that produce changes in the Earth's surface, most commonly those that result in surface displacement (Bürgmann et al., 2000; Massonnet & Feigl, 1998) but also water level changes under flooded vegetation (Jaramillo et al., 2017; H. Liao et al., 2020; T. Liao et al., 2020; Oliver-Cabrera et al., 2021; Wdowinski et al., 2006). However, SAR echoes traveling through the atmosphere are subject to variable delays due to changes in pressure, temperature, and relative humidity in the troposphere. The impacts of tropospheric effects on InSAR observations at different wavelengths have been documented (Bekaert et al., 2015; Fattahi & Amelung, 2015; Sailellah & Fukushima, 2023; H. A. Zebker et al., 1997). Accounting for the propagation delays in transit through the troposphere is still one of the most

Resources: Talib Oliver-Cabrera, Cathleen E. Jones, Marc Simard, Bhuvan Varugu, Saoussen Belhadj-Aissa
Supervision: Cathleen E. Jones, Marc Simard

important challenges faced by scientists using InSAR. Delays caused by these features can be of order tens of centimeters, greatly impacting estimates of surface change.

Different methods of varying sophistication and reliance on external information have been developed to account for tropospheric phase delays (Murray et al., 2019). GNSS stations can be used to estimate and mitigate tropospheric related errors (Byun & Bar-Sever, 2009; Ding et al., 2017; Fernandes et al., 2010; Shamshiri et al., 2020; Williams et al., 1998; Yao et al., 2015). While effective, this method is limited by the spatial distribution of GNSS networks, restricting its applicability to regions with dense station coverage. Another strategy relies on precipitable water vapor (PWV) retrieval products from satellite-based optical sensors such as the Moderate Resolution Imaging Spectroradiometer (MODIS) and the Medium Resolution Imaging Spectrometer (MERIS), which have demonstrated potential to improve InSAR accuracy (Li et al., 2006, 2009). However, these products are constrained by relatively coarse spatial resolution and temporal sampling that often do not coincide with InSAR acquisitions. Additionally, their use is limited to clear-sky conditions, which reduces their utility in many practical scenarios. Corrections based on global weather models like ERA5 from the European Center for Medium-Range Weather Forecasts (ECMWF) have been shown to greatly improve InSAR measurements (Bekaert et al., 2015; Fattahi & Amelung, 2015; Jolivet et al., 2011, 2014; Yu et al., 2018). Nevertheless, the spatial and temporal resolution limitations of the weather models source data hinder accurate estimations of the highly variable condensed water and water vapor clouds, which is often seen in InSAR images (Figure 1). Additionally, statistical methods have been developed to separate tropospheric noise from geophysical signals by exploiting their distinct spatiotemporal characteristics (Ferretti et al., 2001; Tymofyeyeva & Fialko, 2015; Wegmüller et al., 2010). Stochastic models have also been employed to better characterize the variability of atmospheric noise and improve correction accuracy (Cao et al., 2018, 2021). These statistical techniques can be used independently or in combination with external data sources, such as weather models, to enhance the effectiveness of corrections. However, capturing highly variable wet and turbulent delays remains challenging due to their short-lived and rapidly changing nature. As space-borne SARs provide more data, covering more areas and collected more frequently, atmospheric corrections based on the InSAR data itself are increasingly being used. By exploring the volume of data, the temporal and spatial variability of the tropospheric patterns, these methods are able to improve InSAR measurement accuracies (Cohen-Waeber et al., 2018; Ebmeier, 2016; Gaddes et al., 2018; H. Zebker, 2021; M. S. Zebker et al., 2023). However, these methods may not be as effective when data sets are composed of a small number of interferograms or measure large magnitude surface changes in a very short repeat pass interval (Oliver-Cabrera et al., 2021).

Hanssen et al. (1999) extracted water vapor signals from InSAR and compared them to weather radar, satellite imagery, and radiometry observations (e.g., GOES, AVHRR), noting the correlation between weather radar observations and InSAR water vapor phase delay. Based on this, they suggested that InSAR observations could be used for high resolution water vapor mapping. In this work, we build on this idea and implement an InSAR weather phase delay recognition algorithm based on a feature-comparison methodology that uses the reflectivity images collected by the NOAA NEXt-Generation RADar (NEXRAD) weather radar stations (NOAA National Weather Service (NWS) Radar Operations Center (1991), 2024) to identify wet tropospheric delays in L-band InSAR data acquired by the airborne Uninhabited Aerial Vehicle Synthetic Aperture Radar (UAVSAR) (Hensley et al., 2008). The data set comprises of rapid repeat (20–40 min interval) acquisitions in which the InSAR phase measures changes in water level in a Louisiana wetland over a period during which tidal water levels can change tens of centimeters in some parts of the scenes. In this case, eliminating phase outliers based on statistics would also remove the real signal. The NEXRAD data are used to generate a mask to eliminate pixels that are likely contaminated by tropospheric noise, keeping the real signal in uncontaminated areas. The NEXRAD reflectivity is compared to tropospheric delay estimated from GACOS, a weather model and GPS-based atmospheric correction for InSAR (Yu et al., 2018). Additionally, water level gauge data are used to show the overall improvement in water level change (WLC) accuracy from the InSAR time series. Details of the data, method, results, and limitations are given in the sections below.

2. Data Sets

The data sets used in this study consists of two main measurements, UAVSAR InSAR and NEXRAD weather radar, in addition to water level gauge data from the Louisiana Coastwide Reference Monitoring System (CRMS) used for validation of the method's reduction in noise from tropospheric delay. The SAR data were acquired over southern Louisiana for the Delta-X campaign in September 2021 to measure the exchange of water between the

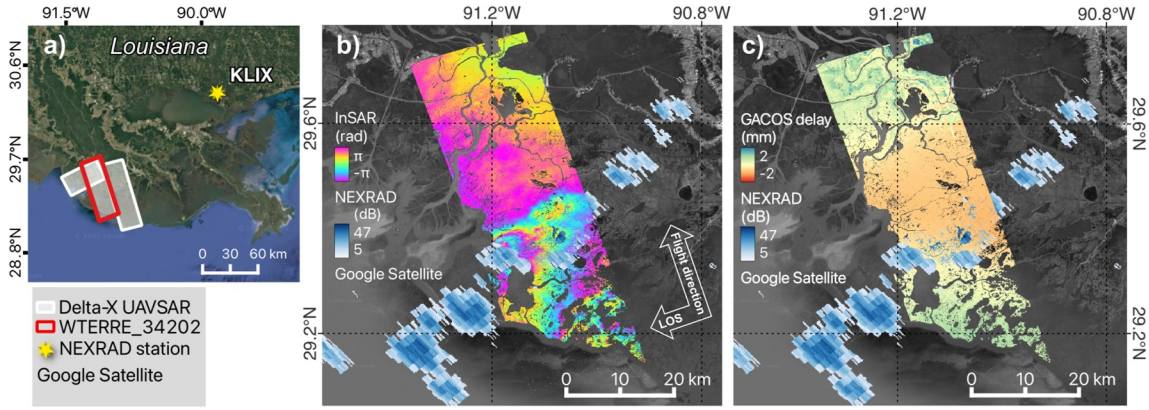

Figure 1. (a) Delta-X UAVSAR coverage. Frame in red shows the scene used for the examples in this manuscript; the other scenes are included in the supplement. The yellow star shows the location of New Orleans KLIX NEXRAD weather radar station. (b) UAVSAR wrapped phase interferogram overlain by a NEXRAD reflectivity image (also shown in Figure S5 of Supporting Information S1). The InSAR map displays a large phase gradient due to wet troposphere and congruent with weather radar observations (±2π radians corresponds to ±12 cm delay at L-band). (c) GACOS-derived (Yu et al., 2018) atmospheric phase delay in mm estimated for the interferogram shown in panel (b). The phase delay from GACOS underestimates the phase gradient observed in InSAR by orders of magnitude.

channels and the wetland (Cortese et al., 2024). The study area and exemplar InSAR and NEXRAD reflectivity maps are shown in Figure 1. The instruments, data, and preprocessing steps are described below.

2.1. InSAR

The InSAR data was acquired over the Atchafalaya and Terrebonne basins with a revisit period of 20–40 min collected during UAVSAR's 5–6-hr flights in September 2021. These flights occurred during the 10 days after Hurricane Ida made landfall at the eastern edge of Terrebonne Bay, a period during which there was substantial and variable wet troposphere in the region. The images were collected from 12.5 km altitude, with an instrument resolution of 0.8 m along the flight path and 1.7 m along the line-of-sight direction. Data were acquired over six swaths from which we selected three representative cases, shown in Figure 1a, which are each 22 km wide and vary in length from 37 to 87 km. The co-registered stack of Single Look Complex (SLC) images for the flightline WTERRE_34202 (swath shown in red in Figure 1a) was selected as the main example in this study (Jones, Simard, et al., 2022). We selected the SLC stack from the 12 September 2021, flight to demonstrate the method because it had extremely high phase outliers in localized areas (Figure 1b). This line was imaged seven times during the flight between times 04:31 and 08:00 UTC. Additional results for data acquired on Sept. 3 (flightline WTERRE_16300) and Sept. 5 (flightline ATCHAF_06309) are included in the supplement.

The SLCs were preprocessed to form interferograms and obtain the interferometric coherence. A multi-look averaging window of 12 by 3 in the azimuth and range directions, respectively, was applied to the interferograms to obtain pixels with spatial resolution of approximately 6 m. Sets of nearest neighbor (NN), NN+1, and NN+2 VV-polarization interferograms were generated using the InSAR Scientific Computing Environment (ISCE) (Rosen et al., 2012) and unwrapped using the statistical-cost, network-flow algorithm for phase unwrapping (SNAPHU) (Chen & Zebker, 2001a, 2001b). Unwrapped phase products were examined to identify phase unwrapping errors and corrected using the phase unwrapping correction algorithm described in Oliver-Cabrera et al. (2021). The mean and standard deviation of the InSAR phase for each pixel in the scene was calculated from the set of all unwrapped interferograms.

2.2. NEXRAD

The NEXRAD network consists of 160 high-resolution Doppler weather radars located in the contiguous United States, Alaska, Hawaii, U.S. territories, and at U.S. military bases (Figure 2a). The data are collected using a 10 cm wavelength S-band radar that scans a 360° azimuthal sweep to sample the atmosphere, with scan times of 4.5, 5, 6, or 10 min depending on the selected product (Figure 2b.). For this work, we use NEXRAD level 2 reflectivity images with 250 m resolution in range and 0.5° in azimuth (NOAA National Weather Service (NWS) Radar Operations Center (1991), 2024) from the KLIX station located in New Orleans, located roughly 150 km

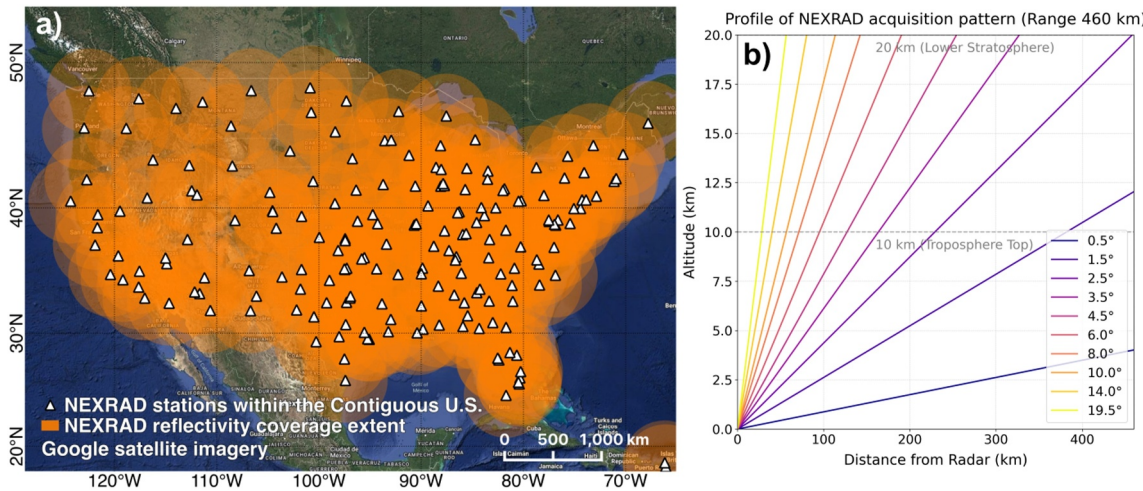

Figure 2. NEXRAD coverage extent (a) orange circles show coverage extent and white triangles show station location. (b) Exemplifies the NEXRAD antenna azimuthal acquisition pattern profile.

from the study area (Figure 1). The images used were those that most closely matched the UAVSAR acquisition times to assign one NEXRAD reflectivity map to each SAR image.

The images were cropped and projected into the UAVSAR radar coordinate grid. To achieve this, we used a georeferenced grid with the same extent and pixel size as the UAVSAR InSAR data. The NEXRAD data were then cropped and resampled to match this grid precisely. Finally, we applied the UAVSAR geometry information to project the resampled NEXRAD data into the UAVSAR radar coordinate system. Because the UAVSAR SAR and the NEXRAD times are not synchronized, a pair of NEXRAD images, one before and one after each UAVSAR acquisition were merged using the maximum reflectivity among the two (Figure S1 in Supporting Information S1). Similarly, to improve weather feature matching, a composite reflectivity image was generated for each NEXRAD acquisition time by taking the highest reflectivity value from all elevations scanned by the station. The merged composite reflectivity images were formed in both time and elevation directions, providing a set of maximum reflectivity maps corresponding to each available interferogram. These maps were then used to create wet-troposphere feature masks by applying a lower-bound threshold of 5 dB. In meteorology, this reflectivity boundary is classified as light precipitation, with 20–30 dB as moderate, and 30–40 dB as heavy (Kumjian, 2018; Rogers & Yau, 1989). This threshold helps minimize false matches caused by noise in the weather radar data. Figure 3 shows the reflectivity images and profiles for four times closely aligned with the SAR acquisitions. Movement of the weather features over the 58 min period is seen.

2.3. CRMS Water Levels

The Louisiana Coastwide Reference Monitoring System (CRMS) is a program designed to monitor and evaluate coastal restoration projects across the state's wetlands. It consists of 390 monitoring sites, each equipped with submersible water level recorders that measure water level elevation hourly (Steyer et al., 2003). In this study, we utilized data from CRMS0301, CRMS0322, and CRMS0329 to assess the impact of tropospheric noise on InSAR phase measurements, with one site serving as a control in a stable, low-noise region. We applied linear interpolation to the CRMS measurements to match the time of the SAR observations. Comparison between InSAR and CRMS stations were performed by estimating a mean InSAR-derived WLC using a 10×10 pixel sample centered around each station location.

3. Methods

The methodology involves an automated one-to-one feature comparison between interferometric phase outliers and weather features extracted from NEXRAD weather radar imagery to identify pixels for which the phase is likely significantly contaminated by noise from wet troposphere delay. However, rather than eliminating single pixels, the workflow considers the overlap of larger regions, called connected components (CCs), that form

10.1029/2025EA004382

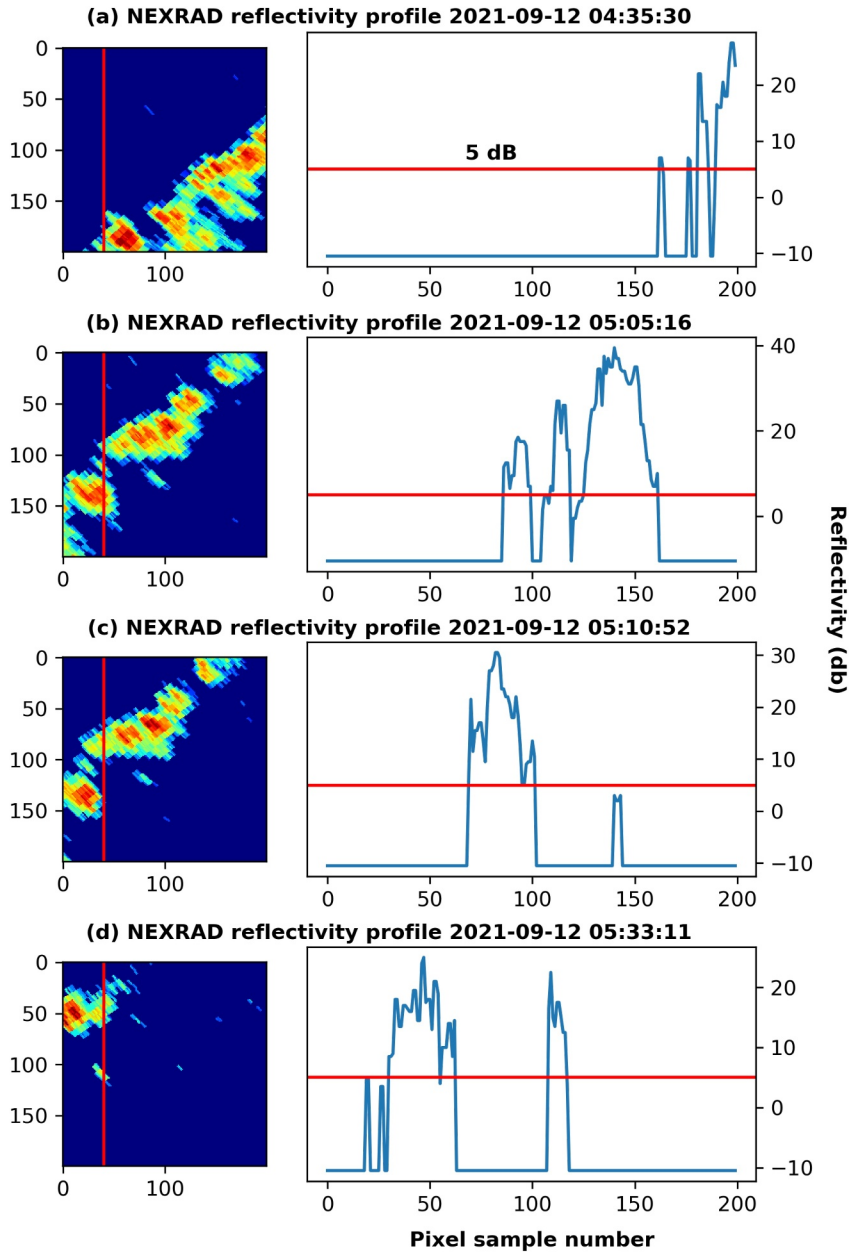

Figure 3. Timelapse progression of reflectivity images and corresponding vertical profiles (plotted over pixels intersecting the red line) from four NEXRAD acquisitions over a 58 min period on 12 September 2021. Panels (a) through (d) present snapshots from the initial time (T04:35:30) to the final time (T05:33:11). The profiles show that most of the cloud reflects well above the 5 dB threshold indicated by the red line.

clusters of pixels with similar phase outlier or NEXRAD reflectivity in order to identify spatially extensive wet troposphere features. The workflow is shown in Figure 4 and described below.

The main weather phase delay recognition algorithm is applied using both the interferograms and the NEXRAD weather mask inputs. The first step is to perform a statistical analysis using the standard deviation of phase from all the interferograms in a stack to define a phase-outlier cut-off threshold. The cut-off threshold is then used to generate a set of phase-outlier masks for each interferogram. The goal of setting the threshold is to extract most of the regions showing relatively high interferometric signal from wet troposphere delays and group them into spatially connected regions called CCs. If the phase outlier corresponds to actual surface change, then we expect only random matches to occur between the weather radar features and interferometric phase. The appropriate

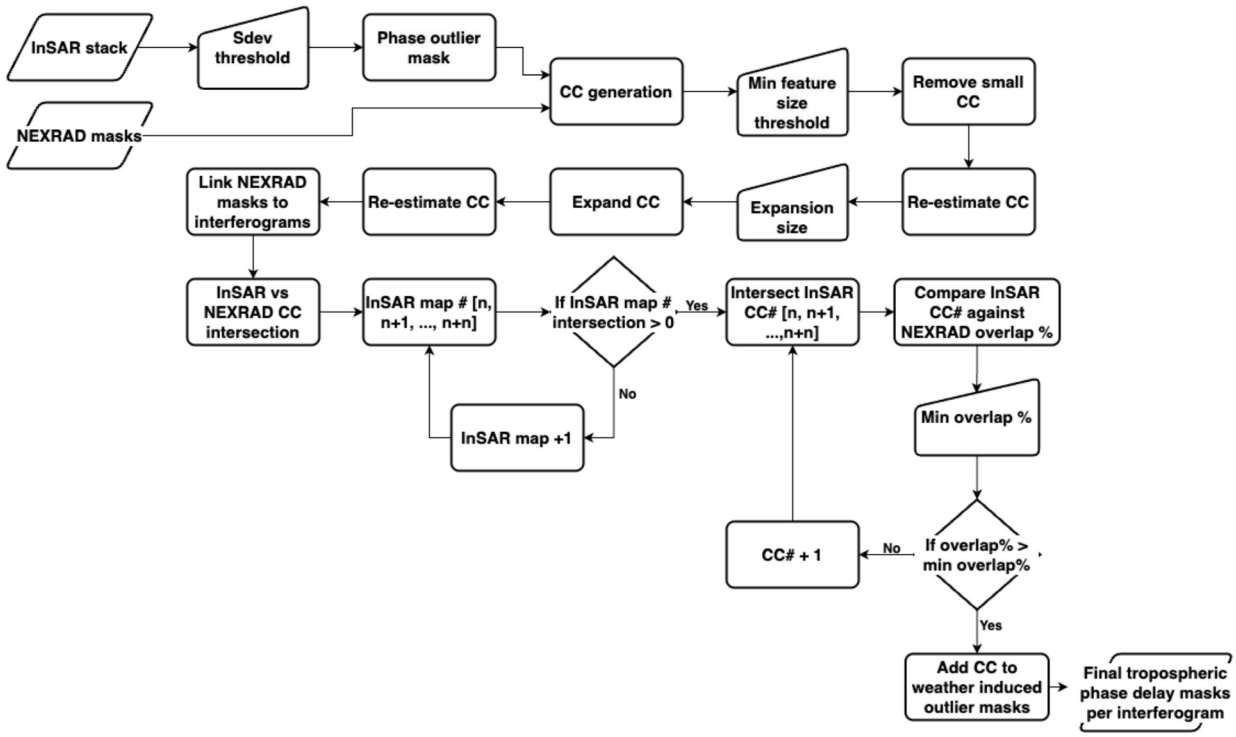

Figure 4. InSAR weather phase delay recognition algorithm workflow. The workflow shown on the left-hand side is applied separately to the reflectivity masks and phase outlier masks to obtain connected components for each. The workflow on the right-hand side identifies patterns in the phase outlier masks that correspond to high NEXRAD reflectivity, indicating likely contamination from wet troposphere delay.

threshold to choose depends on the level of detected surface change and noise in the interferograms. For the case of the examples shown in this work we established a cut-off threshold of $\sigma * 1.5$. This means that all the regions that displayed interferometric phase standard deviation above 1.5 times the average for the entire scene, excluding open water identified using a water mask, are included in a phase outlier mask. A set of NEXRAD CCs are formed using the features in the weather radar mask that are spatially connected.

Two sets of CCs are generated, one for the NEXRAD-derived weather features and one for the interferometric phase outliers. During the CC generation step, small feature removal is performed to keep only features with more than 5,000 pixels. Additionally, each CC is expanded by 10 pixels around its borders to simplify shapes and group nearby outlier pixels. Lastly, we perform a feature-by-feature matching of CCs in the phase outlier mask against the NEXRAD-weather CCs to define shape similarity and to flag regions in the image showing likely atmospheric-induced phase artifacts. We set a minimum spatial overlap threshold of 50% to flag atmospherically induced InSAR phase, meaning that if 50% or more pixels in a phase outlier CC are also in a weather mask CC, then the entire phase outlier CC is identified as being significantly impacted by atmospheric noise. This threshold can be adjusted based on user analysis. Finally, a set of binary masks with values 0 for regions with no weather feature matches and 1 for areas with matching weather features are generated, one for each interferogram. Figure 5 shows an example of the algorithm steps performed for one interferogram.

4. Results

4.1. Wet Troposphere Masks

Results from the algorithm implementation show that the method can identify most of the tropospheric-induced phase delay (Figure 6). The example from flight line WTERRE_34202 shows large InSAR signals noticeable for their red and blue colors in Figure 6a. The majority of the matched wet-tropospheric delay exceed $\pm 2\pi$ radian phase, which corresponds to $\sim \pm 12$ cm of range delay for an L-band sensor. The NEXRAD reflectivity shows cloud features in green-yellow-red colors that align with the observed InSAR phase delays, reaching more than 40 dB in some cases. Regions of clear skies in the NEXRAD data set are shown in dark blue (Figure 6b). Often,

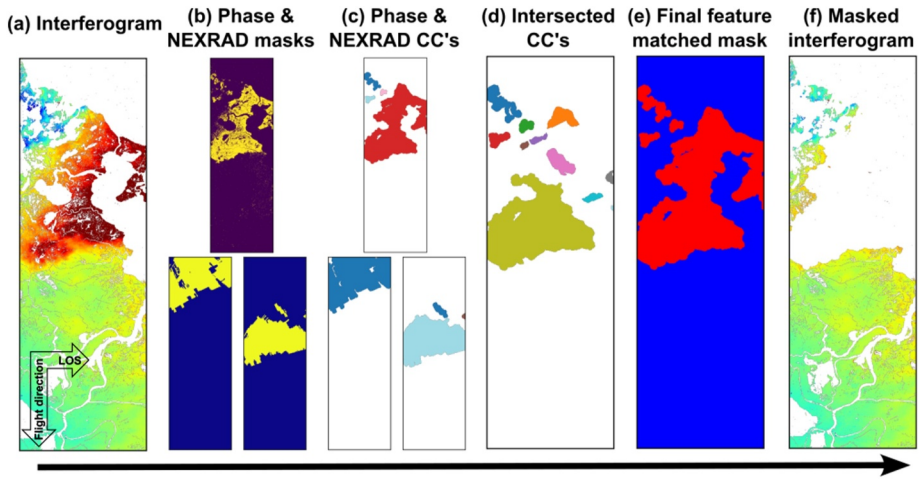

Figure 5. Single interferogram example from UAVSAR flightline WTERRE_34202 showing each step from the feature comparison algorithm. The algorithm flow is arranged from left to right, starting with the original unwrapped interferogram to the left and proceeding to the resulting mask and masked interferogram on the right side. (a) Raw unwrapped interferogram. (b) Masks derived using phase standard deviation threshold for (top) InSAR with the regions that are above the phase standard deviation threshold shown in yellow, and (bottom) the NEXRAD regions that have reflectivity above 5 dB shown in yellow for the two acquisition times of the images forming the interferogram. (c) Connected components (CCs) for (top) the thresholded InSAR phase mask in panel (b), and (bottom) the NEXRAD masks in panel (b). Each color represents a region of adjacent pixels (a single CC). (d) InSAR phase CCs intersecting NEXRAD CCs obtained from feature matching. Different colors represent regions of adjacent pixels. (e) Final phase mask showing in red areas marked as affected by tropospheric phase delay. (f) Interferogram after masking the areas affected by tropospheric phase delay.

when looking at satellite-based interferograms (e.g., Sentinel-1, ALOS2/4 etc.), expected surface change is in the range of few centimeters or even millimeters, making large tropospheric phase delays (typically in the order of tens of centimeters) more detectable since they exceed the expected measurable signal. However, in cases like the ones presented here, where the interferograms are detecting WLC dynamics leveraged by rapid repeat passes, tropospheric phase delays can be of the same order as the expected WLC, making them difficult to detect and separate. By matching weather radar reflectivity to the interferograms, it becomes evident that many of those large-scale phase signals are produced by the presence of wet troposphere delay (Figure 6d). Additional examples of the method applied to flightlines ATCHAF_06309 and WTERRE_16300 are shown in the Figures S2 and S3 in Supporting Information S1, respectively.

4.2. Comparison With Water Level Gauge Data

We generated a WLC time series for flightline WTERRE_34202 and compared it to in situ measurements from CRMS water level gauges, as described in Section 2.3. To assess the impact of troposphere-induced phase delay on the InSAR time series, we selected representative gauges from both wet troposphere weather feature affected and unaffected regions. Specifically, we analyzed data from CRMS0301 and CRMS0322, located in impacted areas (Figures 7a and 7b), and CRMS0329, situated in an unaffected region (Figure 7c) by wet tropospheric effects (Figure 7).

A detailed look at the comparison between InSAR WLC time series and CRMS water level gauges shows visible jumps at times 05:35 and 05:06 for the examples shown in Figures 7a and 7b, respectively. Figure 6 shows that all interferograms formed using images acquired at those times show large phase delays that were identified as being induced by wet troposphere. By removing those two times steps from the time series, the root mean square error (RMSE) dropped from 5.29 to 3.1 cm for case (a) and from 7.7 to 4.4 cm for case (b). For comparison, the example shown in Figure 7c is for a gauge located outside the wet tropospheric-impacted region ("clear sky"). In this case, the RMSE of 2.1 cm is much lower than for the other two examples and changes little when removing the time steps since it is located in a clear sky area.

10.1029/2025EA004382

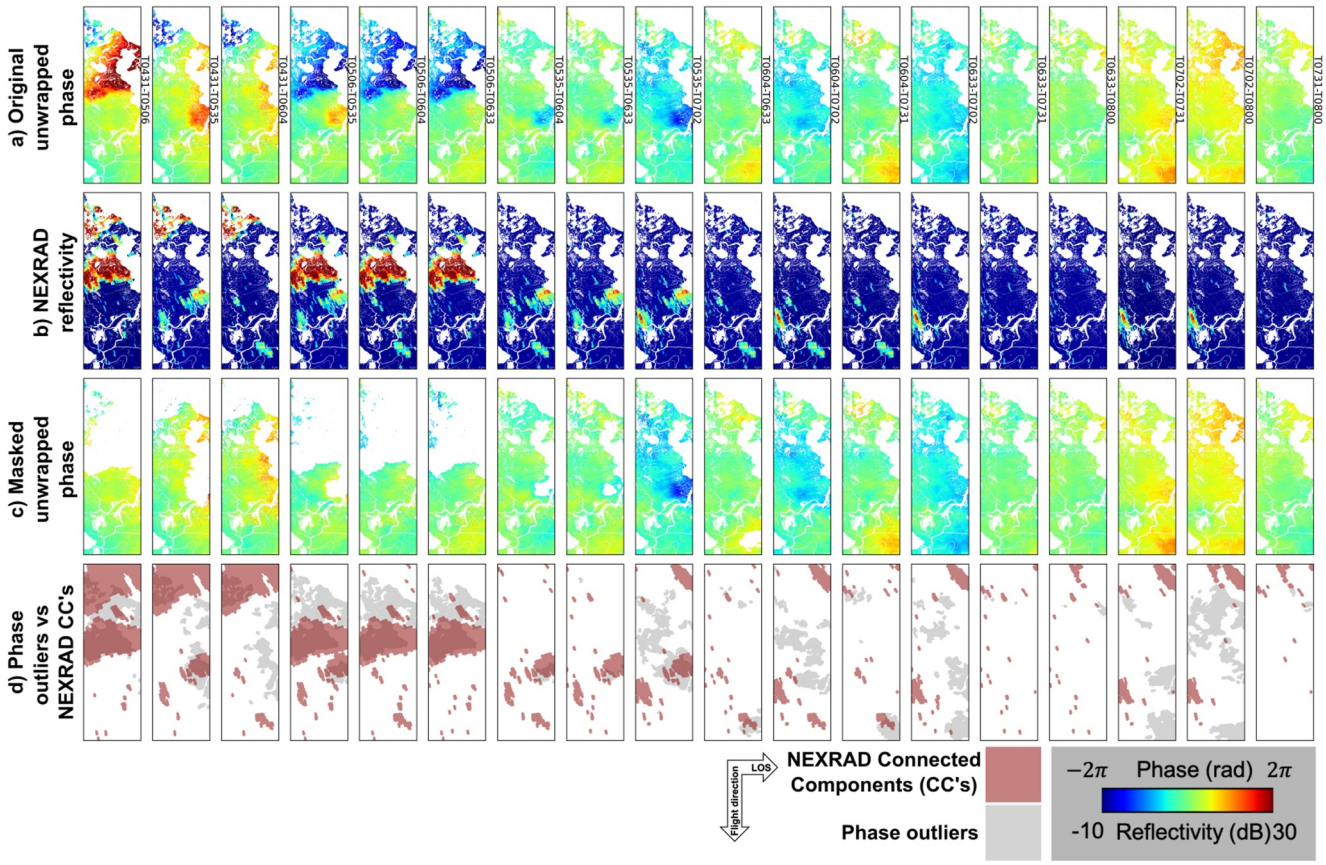

Figure 6. Full set of unwrapped interferograms (a) from UAVSAR flight line WTERRE_34202 acquired on 12 September 2021. The color scale ranges from −2π (blue) to 2π (red), as shown in the bottom right corner. Panel (b) displays NEXRAD composite reflectivity maps, ranging from −10 to 30 dB (color scale at bottom right), projected into the UAVSAR grid and merged to match the two InSAR acquisition times. Unwrapped interferograms masked using the detected tropospheric-phase delay regions are shown in panel (c) and the extracted phase outliers connected components (CCs) as well as the NEXRAD CCs used to form the mask of weather induced phase delay are presented in panel (d).

5. Discussion

Throughout this work, we introduce a novel algorithm designed to enhance the detection of tropospheric phase delays in interferometric products by integrating weather radar data. Weather radar provides valuable information due to its extensive spatial coverage, availability across various locations worldwide, and ability to capture rapid tropospheric variations, particularly those associated with the wet troposphere. As illustrated in Figure 1, commonly used atmospheric models for InSAR corrections, such as ERA5 and GACOS, while robust and widely utilized, lack the temporal and spatial resolution necessary to capture these fine-scale atmospheric variations. This limitation is evident in Figure 1b, where the observed tropospheric feature induces a phase delay of approximately 47 cm (25 radians), whereas for the same site, GACOS estimates indicate a delay of only ∼2 mm, entirely missing the tropospheric anomaly. While the tropospheric phase delay recognition algorithm detected the majority of regions with wet troposphere-induced phase delay (Figure 6c), some of them still remain. Such is the case for interferogram T05:35-T07:02 (see Figure 6a) where the interferometric signal located at the center of the interferogram in blue color was not detected even though the same feature was identified for all the other interferograms in the series. This could be due to a couple of reasons: First, the overlap of features may be affected by differences in radar viewing geometry and spatial resolution between the SAR sensor and the weather radar. While UAVSAR, a side-looking airborne instrument, images its target from an overhead diagonal perspective, NEXRAD collects data from the ground in an azimuthal pattern (Figure 2). These differing acquisition angles can lead to variations in both the shape and location of the atmospheric feature being observed. Using multiple NEXRAD stations can improve feature matching, especially when the study area is centrally located and observable from several stations at different angles. However, stations that are located far from the study area lose

10.1029/2025EA004382

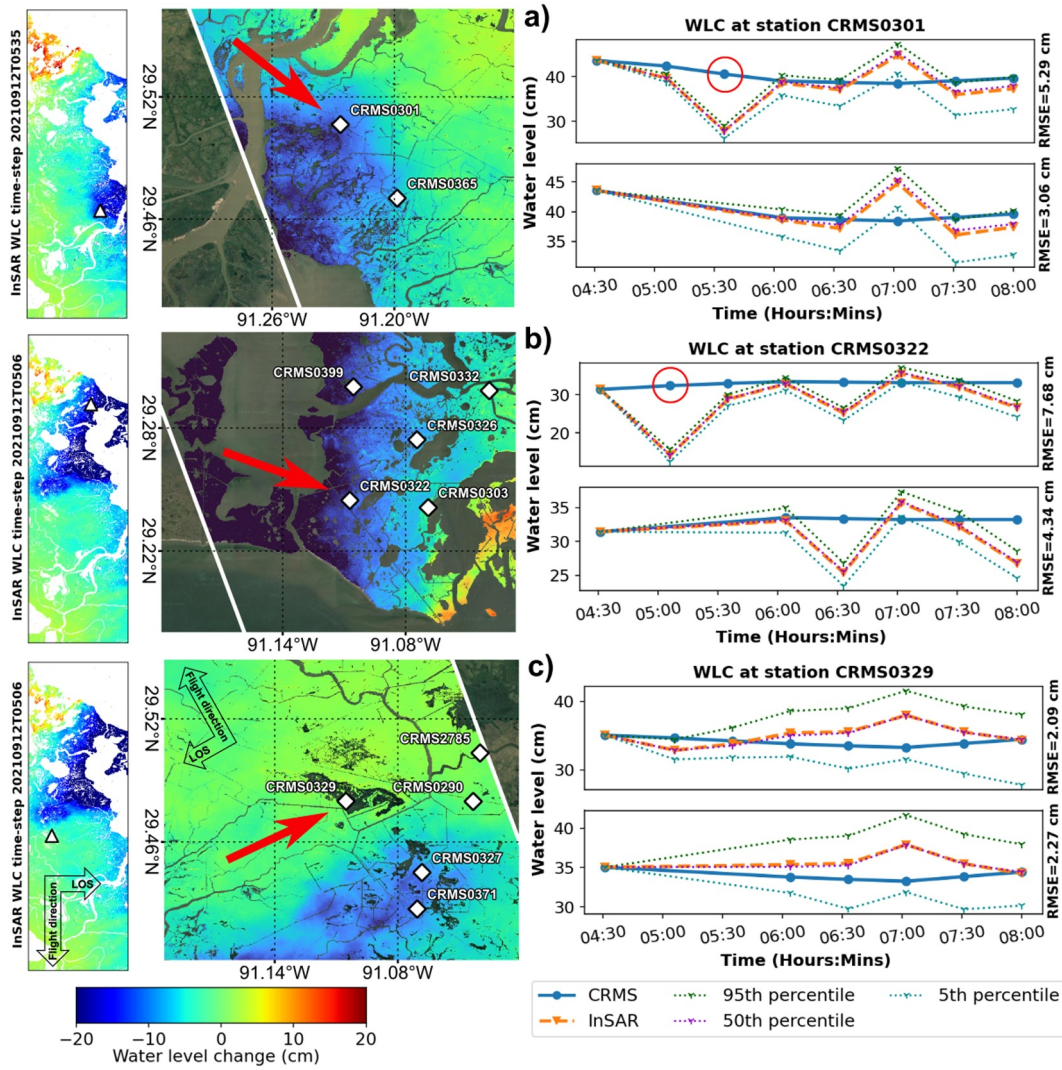

Figure 7. InSAR time series of water level change (WLC) compared to measurements at CRMS in situ water level gauges. The red arrows indicate the location of the water level stations for which data are shown in the plots. The plots to the right of each map show the extracted time series for both InSAR-derived WLC and the water level gauge. There are two WLC time series plot for each example site (a–c). The upper plot displays the unmodified InSAR time series, including the tropospheric noise, with the affected timesteps highlighted by red circles. The bottom plot shows the InSAR time series after dropping time-steps 05:06 and 05:35, which contain most of the wet tropospheric delay in this flightline. A mean WLC sample over a 10 × 10 window centered at the CRMS station was used to generate the InSAR time series.

visibility particularly of tropospheric features at lower altitudes due to the azimuthal acquisition pattern (Figure S4 in Supporting Information S1). Connected component grouping and/or overlapping tolerances may need to be adjusted to account for these differences. Connected component grouping can be modified by using different phase outlier cut-off thresholds or by forcing the separation of a single CC into two or more CCs by implementing a mask or an image processing morphological operation (e.g., erosion). The overlapping tolerances can be adjusted by simple relaxing or increasing the minimum spatial overlap threshold between phase and weather radar components. Second, real InSAR phase change from the process of interest (e.g., WLC or surface displacement) and troposphere-induced phase can display similar magnitudes and overlap spatially. This can result in a large feature that includes the combination of phase changes and may require additional post-processing to be resolved. The example in Figure 8 shows that the troposphere-induced phase delay overlaps with what seems to be WLC patterns in the upper part of the interferogram (Figure 8a). The tropospheric phase delay recognition algorithm in this case extracted both the region of WLC as well as the phase delay due to troposphere presence and generalized

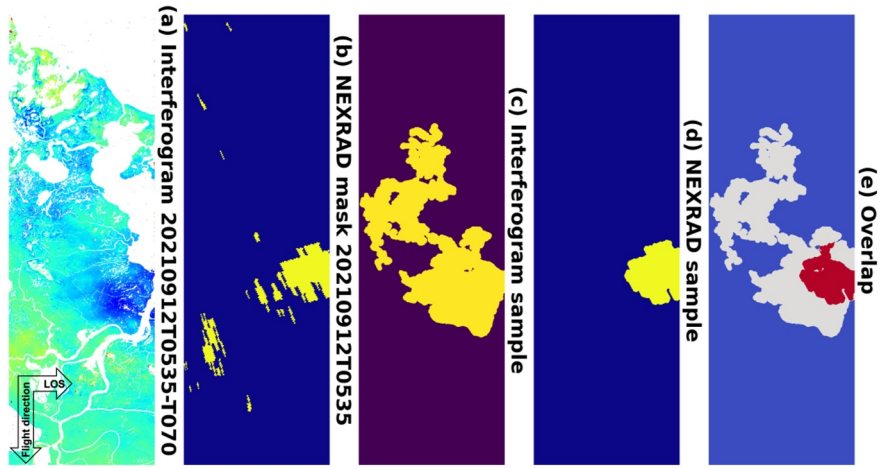

Figure 8. Example of connected component (CC) mismatch. Maps shown from left to right are: (a) Interferogram for time T05:35-T0702, (b) NEXRAD weather radar mask for time T05:35, (c) extracted phase outlier mask for interferogram (a, d) NEXRAD CC to be compared against feature (c, e) overlap between features (c, d).

them into one very large CC (Figure 8c) that did not pass the overlap threshold (Figure 8e), thus was not recognized as a potential tropospheric noise feature.

Although the algorithm correctly identified most of the tropospheric-induced phase delay, a careful review is still necessary to refine thresholds to ensure the best possible results. One could also consider discarding the SAR acquisition at time 05:35 to remove the residual tropospheric feature shown in Figure 6a. However, this is not recommended here because there were only a few Delta-X InSAR acquisitions over a very short repeat-pass interval, so the cloud-free regions of the images provide useful information on patterns of water flows through wetlands and canals. Discarding an entire scene because of spatially limited phase noise is not always desirable. It is anticipated that satellite-InSAR measurements will exhibit a higher spatial correlation between phase outliers and the wet troposphere. This expectation arises from the inherent characteristics of satellite-based measurements, which commonly feature reduced variability of the acquisition geometry compared to those obtained from UAVSAR, for which the incidence angle varies from ∼22° in the near range to ∼67° in the far range. Nonetheless, the persistent challenge of the rapidly moving wet troposphere remains, posing a significant issue that new missions such as NISAR will face, particularly in tropical and coastal regions.

Results presented in this work demonstrate that NEXRAD data exhibits strong spatial correlation with tropospheric delay patterns observed in the UAVSAR data set. However, weather radar alone may not always be sufficient to fully characterize or isolate tropospheric noise. This limitation arises from fundamental differences in the type of information each system provides. InSAR-derived tropospheric delay is primarily influenced by atmospheric water vapor, whereas NEXRAD primarily detects hydrometeors such as rain, hail, and snow. As a result, tropospheric delay may be present in InSAR observations without a corresponding signal in NEXRAD data, particularly under non-precipitating conditions. Nonetheless, during the active phases of the precipitation lifecycle, the two data sets tend to exhibit a high degree of correlation (Hanssen et al., 1999; Kinoshita et al., 2013). To better understand the relationship between the weather radar reflectivity and interferometric phase, we show in Figure 9a profile plot of NEXRAD reflectivity and InSAR phase over a region exhibiting a distinct atmospheric pattern. The tropospheric phase delay observed in the interferogram (Figure 9a) exceeds 7.5 radians (∼14.2 cm), while the reflectivity in Figure 9c reaches nearly 40 dB. The profile plot shows that the peak phase delay matches the weather radar peak reflectivity (Figure 9b). Precipitation rates derived from the NEXRAD measurements are up to 6 mm/hr. A detailed examination of interferogram T0431-T0506 (Figure 9a) reveals that the same cloud feature was captured twice as it shifted during the time interval between the two SAR acquisitions used to generate the interferogram. The cloud is first captured in the upper left corner displaying phase in negative radian values (shown in blue colors) and appear again toward the upper center of the interferogram but here with positive phase (in red colors). The weather radar reflectivity measurements show comparable values. This same pattern is also visible in Figures 5, 6a and 6b (e.g., T0431-T0535 and T0506-T0535). This illustration aids in understanding the connection between tropospheric phase delay and the presence of

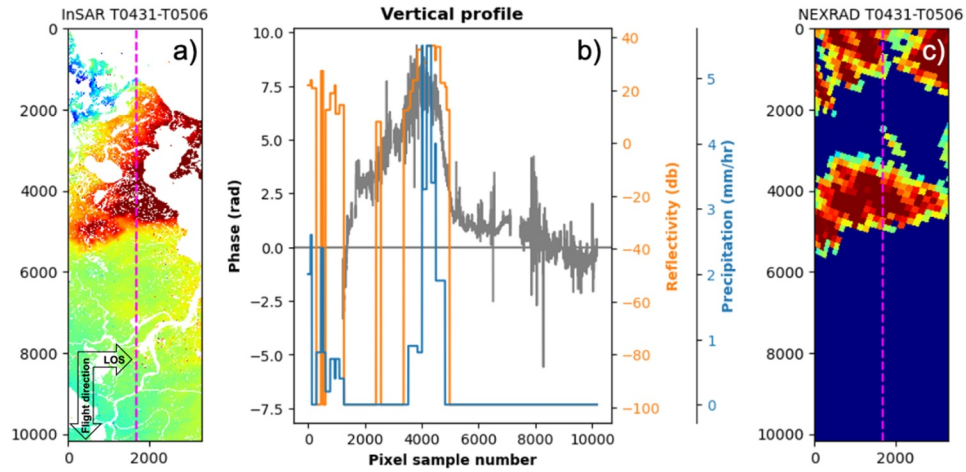

Figure 9. InSAR and NEXRAD reflectivity profiles sample at the magenta dashed line location (b). Gray profile shows phase in radians, orange profile reflectivity in decibels and blue precipitation rate in mm/hr. Maps (a, c) show the interferogram and reflectivity at times T0431-T0506, respectively.

clouds, as well as the correlation with cloud-water content. Furthermore, it provides insight on the impact of fast moving wet-troposphere and its effect on rapid repeated SAR measurements.

Additionally, detailed examination of the InSAR phase profile shows sharp peaks observed at approximately pixel samples 6,400 and 8,000. These peaks likely correspond to detected WLC, since they are located near an open water channel that feeds the wetlands and are located outside of the region impacted by wet tropospheric delay, having no reflectivity or precipitation recorded. Using the phase outliers removed from Figure 6c, we analyzed phase delay values by grouping them according to reflectivity ranges. Our findings indicate that for reflectivity levels between 5 and 20 dB, corresponding to light precipitation, the most frequent phase delay values range from 1 to 2 radians. In the 20–30 dB range, associated with moderate precipitation, the predominant phase delay values fall between 3 and 3.5 radians. For higher reflectivity values of 30–40 dB, indicative of heavy precipitation, the most common phase delay values range from 3.5 to 5.5 radians. While modeling and removing the observed tropospheric delay may be desirable, it is particularly challenging for cases of study like the one presented here in which the time series are very short, making it difficult to isolate a period with clean InSAR phase measurements that could serve as a reliable reference. Additionally, the magnitude of the tropospheric phase delay is often comparable to the expected water level changes in the region, complicating the separation of atmospheric effects from actual surface changes. Compounding the issue, the study area is a wetland dominated by emergent vegetation and is notoriously difficult to access. As a result, there are no reliable water level gauges inside the wetland region to validate any atmospheric correction models. This remains an open question for future work, perhaps over less dynamic regions. The work by Murray et al. (2019) provides a comprehensive review of various methodologies and data sets available for correcting atmospheric phase delays. Although the authors discussed the potential use of weather radar data, such as NEXRAD, they emphasize its limitation to United States (U.S.) territories and its inability to directly detect tropospheric wet delay. Contrary to what the authors reported, our results demonstrate a strong correlation between wet tropospheric features and InSAR phase delay (Figure 9). Furthermore, while the NEXRAD system is only available for the U.S. territory, similar systems are available around the globe, including the Canadian Weather Radar Network (CWRN), the United Kingdom Met Office Radar Network, and the European Operational Program for the Exchange of Weather Radar Information, among others. These findings, along with the feasibility of implementing the proposed approach in various countries, suggest that incorporating weather radar data as a correction layer for InSAR can support detection of atmospheric delays. This is particularly beneficial in regions with highly dynamic atmospheric conditions, where weather models or GNSS data may lack sufficient temporal or spatial resolution (Murray et al., 2019).

6. Conclusions

We unequivocally demonstrated the impact of wet troposphere on InSAR phase measurements using corresponding spatial patterns observed with the NEXRAD weather radar reflectivity and phase outliers. Our wet

troposphere recognition method leveraged weather radar information to improve interpretation of InSAR phase signals, and allows us to automatically identify and remove unreliable InSAR observations within an interferogram, with the potential to keep the information in reliable areas. This was demonstrated on a data set where the phase change is due to WLC, a case in which large phase changes could easily be the real signal of interest. Observed troposphere-induced phase delays reach up to 25 radians for the example data shown, which translates to approximately 47 cm of noise on a displacement or WLC signal. Identification of regions impacted by tropospheric delay is thus critical when using L-band InSAR measurement of surface elevation change. The weather radar matching method was able to detect regions impacted by wet troposphere and mask them out, reducing measurement errors without affecting measurements in unimpacted areas. A comparison against weather model delay derived from GACOS, a standard method for InSAR atmospheric noise correction, showed that it has insufficient temporal and spatial resolution to address wet troposphere phase delays, which can alter much more quickly than is captured by the standard methods. While the method suggested in this work was specifically developed for rapid-repeat InSAR products, it can be used to identify phase delays due to wet troposphere observed by other InSAR instruments, including the L-band NISAR and ALOS2/4, and potentially other frequency SARs (C-band Sentinel-1; X-band TerraSAR-X) also. Importantly, our approach provides an additional layer of atmospheric information that will help improve InSAR estimations in cases where weather models are unable to capture small-scale atmospheric patterns. This is particularly important in coastal and tropical areas where wet troposphere is common.

Conflict of Interest

The authors declare no conflicts of interest relevant to this study.

Data Availability Statement

The data used in this study is part of the Delta-X mission and can be found at the Oak Ridge National Laboratory Distributed Active Archive Center (OARNL DAAC) under the name Delta-X UAVSAR L1B Interferometric products (doi.org/10.3334/ORNLDAAC/1979) (Jones, Simard, et al., 2022) and L2 Interferometric products (doi.org/10.3334/ORNLDAAC/2057) (Jones, Oliver-Cabrera et al., 2022). The ISCE2 software is available on Github at https://github.com/isce-framework/isce2 (Rosen et al., 2012). NEXRAD Reflectivity maps were generated using NOAA Weather and Climate toolkit, available at www.ncdc.noaa.gov/wct (NOAA National Weather Service (NWS) Radar Operations Center (1991), 2024). CRMS water level data can be found at, www.lacoast.gov/crms (Coastal Protection and Restoration Authority (CPRA) of Louisiana., 2024).

Acknowledgments
This work was performed at the Jet Propulsion Laboratory, California Institute of Technology, under contract with the National Aeronautics and Space Administration (NASA). The NASA Delta-X project is funded by the Science Mission Directorate's Earth Science Division through the Earth Venture Suborbital-3 Program NNH17ZDA001N-EVS3. The authors thank Prof. Chuntao Liu for aiding with his feedback in the initial interpretation of NEXRAD data and generously granting access to his NOAA MRMS data archive during early stages of this research.

References

Bamler, R., & Hartl, P. (1998). Synthetic aperture radar interferometry. In *Inverse problems* (Vol. 14(4), R1–R54. https://doi.org/10.1088/0266-5611/14/4/001

Bekaert, D. P. S., Walters, R. J., Wright, T. J., Hooper, A. J., & Parker, D. J. (2015). Statistical comparison of InSAR tropospheric correction techniques. *Remote Sensing of Environment*, *170*, 40–47. https://doi.org/10.1016/j.rse.2015.08.035

Bürgmann, R., Rosen, P. A., & Fielding, E. J. (2000). Synthetic aperture radar interferometry to measure Earth's surface topography and its deformation. *Annual Review of Earth and Planetary Sciences*, *28*(1), 169–209. https://doi.org/10.1146/annurev.earth.28.1.169

Byun, S. H., & Bar-Sever, Y. E. (2009). A new type of troposphere zenith path delay product of the international GNSS service. *Journal of Geodesy*, *83*(3–4), 367–373. https://doi.org/10.1007/s00190-008-0288-8

Cao, Y., Jónsson, S., & Li, Z. (2021). Advanced InSAR tropospheric corrections from global atmospheric models that incorporate spatial stochastic properties of the troposphere. *Journal of Geophysical Research: Solid Earth*, *126*(5). https://doi.org/10.1029/2020JB020952

Cao, Y., Li, Z., Wei, J., Hu, J., Duan, M., & Feng, G. (2018). Stochastic modeling for time series InSAR: With emphasis on atmospheric effects. *Journal of Geodesy*, *92*(2), 185–204. https://doi.org/10.1007/s00190-017-1055-5

Chen, C. W., & Zebker, H. A. (2001a). Network approaches to two-dimensional phase unwrapping: Intractability and two new algorithms: Erratum. *Journal of the Optical Society of America*, *18*(5), 1192. https://doi.org/10.1364/josaa.18.001192

Chen, C. W., & Zebker, H. A. (2001b). Two-dimensional phase unwrapping with use of statistical models for cost functions in nonlinear optimization. *Journal of the Optical Society of America*, *18*(2), 338. https://doi.org/10.1364/josaa.18.000338

Coastal Protection and Restoration Authority (CPRA) of Louisiana. (2024). Coastwide reference monitoring system-wetlands monitoring data [Dataset]. *Coastal Information Management System (CIMS)*. database Retrieved from http://cims.coastal.louisiana.gov

Cohen-Waeber, J., Bürgmann, R., Chaussard, E., Giannico, C., & Ferretti, A. (2018). Spatiotemporal patterns of precipitation-modulated landslide deformation from independent component analysis of InSAR time series. *Geophysical Research Letters*, *45*(4), 1878–1887. https://doi.org/10.1002/2017GL075950

Cortese, L., Donatelli, C., Zhang, X., Nghiem, J. A., Simard, M., Jones, C. E., et al. (2024). Coupling numerical models of deltaic wetlands with AirSWOT, UAVSAR, and AVIRIS-NG remote sensing data. *Biogeosciences*, *21*(1), 241–260. https://doi.org/10.5194/bg-21-241-2024

Ding, W., Teferle, F. N., Kazmierski, K., Laurichesse, D., & Yuan, Y. (2017). An evaluation of real-time troposphere estimation based on GNSS Precise Point Positioning. *Journal of Geophysical Research: Atmospheres*, *122*(5), 2779–2790. https://doi.org/10.1002/2016JD025727

Ebmeier, S. K. (2016). Application of independent component analysis to multitemporal InSAR data with volcanic case studies. *Journal of Geophysical Research: Solid Earth*, *121*(12), 8970–8986. https://doi.org/10.1002/2016JB013765

Fattahi, H., & Amelung, F. (2015). InSAR bias and uncertainty due to the systematic and stochastic tropospheric delay. *Journal of Geophysical Research: Solid Earth*, *120*(12), 8758–8773. https://doi.org/10.1002/2015JB012419

Fernandes, M. J., Lázaro, C., Nunes, A. L., Pires, N., Bastos, L., & Mendes, V. B. (2010). GNSS-derived path delay: An approach to compute the wet tropospheric correction for coastal altimetry. *IEEE Geoscience and Remote Sensing Letters*, *7*(3), 596–600. https://doi.org/10.1109/LGRS.2010.2042425

Ferretti, A., Prati, C., & Rocca, F. (2001). Permanent scatterers in SAR interferometry. *IEEE Transactions on Geoscience and Remote Sensing*, *39*(1), 8–20. https://doi.org/10.1109/36.898661

Gaddes, M. E., Hooper, A., Bagnardi, M., Inman, H., & Albino, F. (2018). Blind signal separation methods for InSAR: The potential to automatically detect and monitor signals of volcanic deformation. *Journal of Geophysical Research: Solid Earth*, *123*(11), 10226–10251. https://doi.org/10.1029/2018JB016210

González, P. J. (2024). Interferometric synthetic aperture radar (InSAR). In E. Chaussard, C. Jones, J. A. Chen, & A. Donnellan (Eds.), *Remote sensing for characterization of geohazards and natural Resources. Springer remote sensing/photogrammetry*. Springer. https://doi.org/10.1007/978-3-031-59306-2_3

Hanssen, R. F., Weckwerth, T. M., Zebker, H. A., & Klees, R. (1999). High-resolution water vapor mapping from interferometric radar measurements. *Science*, *283*(5406), 1297–1299. https://doi.org/10.1126/science.283.5406.1297

Hensley, S., Wheeler, K., Sadowy, G., Jones, C., Shaffer, S., Zebker, H., et al. (2008). The UAVSAR instrument: Description and first results. In *2008 IEEE radar conference, RADAR 2008* (pp. 0–5). https://doi.org/10.1109/RADAR.2008.4720722

Jaramillo, F., Brown, I., Castellazzi, P., Espinosa, L., Guittard, A., Hong, S.-H., et al. (2017). Assessment of hydrologic connectivity in an ungauged wetland with InSAR observations. *Environmental Research Letters*, *13*(2), 024003. https://doi.org/10.1088/1748-9326/aa9d23

Jolivet, R., Agram, P. S., Lin, N. Y., Simons, M., Doin, M., Peltzer, G., & Li, Z. (2014). Improving InSAR geodesy using global atmospheric models. *Journal of Geophysical Research: Solid Earth*, *119*(3), 2324–2341. https://doi.org/10.1002/2013JB010588.Received

Jolivet, R., Grandin, R., Lasserre, C., Doin, M. P., & Peltzer, G. (2011). Systematic InSAR tropospheric phase delay corrections from global meteorological reanalysis data. *Geophysical Research Letters*, *38*(17), 1–6. https://doi.org/10.1029/2011GL048757

Jones, C., Oliver-Cabrera, T., Simard, M., & Lou, Y. (2022). Delta-X: UAVSAR L2 interferometric products, MRD, Louisiana, 2021 [Dataset]. *ORNL Distributed Active Archive Center*. https://doi.org/10.3334/ORNLDAAC/2057

Jones, C., Simard, M., Lou, Y., & Oliver-Cabrera, T. (2022). Delta-X: UAVSAR L1 single look Complex (SLC) stack products, MRD, Louisiana, 2021 [Dataset]. *ORNL Distributed Active Archive Center*. https://doi.org/10.3334/ORNLDAAC/1984

Kinoshita, Y., Shimada, M., & Furuya, M. (2013). InSAR observation and numerical modeling of the water vapor signal during a heavy rain: A case study of the 2008 Seino event, central Japan. *Geophysical Research Letters*, *40*(17), 4740–4744. https://doi.org/10.1002/grl.50891

Kumjian, M. R. (2018). Weather radars. In C. Andronache (Ed.), *Remote sensing of clouds and precipitation* (pp. 15–63). Springer International Publishing. https://doi.org/10.1007/978-3-319-72583-3_2

Li, Z., Fielding, E. J., & Cross, P. (2009). Integration of InSAR time-series analysis and water-vapor correction for mapping postseismic motion after the 2003 Bam (Iran) earthquake. *IEEE Transactions on Geoscience and Remote Sensing*, *47*(9), 3220–3230. https://doi.org/10.1109/TGRS.2009.2019125

Li, Z., Fielding, E. J., Cross, P., & Muller, J. P. (2006). Interferometric synthetic aperture radar atmospheric correction: Medium resolution imaging spectrometer and advanced synthetic aperture radar integration. *Geophysical Research Letters*, *33*(6). https://doi.org/10.1029/2005GL025299

Liao, H., Wdowinski, S., & Li, S. (2020). Regional-scale hydrological monitoring of wetlands with Sentinel-1 InSAR observations: Case study of the South Florida Everglades. *Remote Sensing of Environment*, *251*(February), 112051. https://doi.org/10.1016/j.rse.2020.112051

Liao, T., Simard, M., Denbina, M., & Lamb, M. P. (2020). Monitoring water level change and seasonal vegetation change in the coastal wetlands of Louisiana using L-band time-series. *Remote Sensing*, *12*(15), 2351. https://doi.org/10.3390/rs12152351

Massonnet, D., & Feigl, K. L. (1998). Radar interferometry and its application to changes in the Earth's surface. *Reviews of Geophysics*, *4*(36), 441–500. https://doi.org/10.1029/97rg03139

Murray, K. D., Bekaert, D. P. S., & Lohman, R. B. (2019). Tropospheric corrections for InSAR: Statistical assessments and applications to the Central United States and Mexico. *Remote Sensing of Environment*, *232*(111326). 111326. https://doi.org/10.1016/j.rse.2019.111326

NOAA National Weather Service (NWS) Radar Operations Center. (1991). 2024 NOAA next generation radar (NEXRAD) level 2 base data [Dataset]. *NOAA National Centers for Environmental Information*. https://doi.org/10.7289/V5W9574V

Oliver-Cabrera, T., Jones, C. E., Yunjun, Z., & Simard, M. (2021). InSAR phase unwrapping error correction for rapid repeat measurements of water level change in wetlands. *IEEE Transactions on Geoscience and Remote Sensing*, *60*, 1–15. https://doi.org/10.1109/TGRS.2021.3108751

Rogers, R. R., & Yau, M. K. (1989). *A short course in cloud physics* (3rd ed.). Pergamon Press.

Rosen, P. A., Gurrola, E., Sacco, G. F., & Zebker, H. (2012). The InSAR scientific computing environment. Proceedings of the European conference on synthetic aperture radar [Software]. *EUSAR*, 730–733. https://ieeexplore.ieee.org/abstract/document/6217174

Sailellah, S. N., & Fukushima, Y. (2023). Comparison of tropospheric delay correction methods for InSAR analysis using a mesoscale meteorological model: A case study from Japan. *Earth Planets and Space*, *75*(1), 18. https://doi.org/10.1186/s40623-023-01773-z

Shamshiri, R., Motagh, M., Nahavandchi, H., Haghshenas Haghighi, M., & Hoseini, M. (2020). Improving tropospheric corrections on large-scale Sentinel-1 interferograms using a machine learning approach for integration with GNSS-derived Zenith Total Delay (ZTD). *Remote Sensing of Environment*, *239*, 111608. https://doi.org/10.1016/j.rse.2019.111608

Steyer, G. D., Sasser, C. E., Visser, J. M., Swenson, E. M., Nyman, J. A., & Raynie, R. C. (2003). A proposed coast-wide reference monitoring system for evaluating wetland restoration trajectories in Louisiana. In B. D. Melzian, V. Engle, M. McAlister, S. Sandhu, & L. K. Eads (Eds.), *Coastal monitoring through partnerships: Proceedings of the fifth symposium on the Environmental Monitoring and Assessment Program (EMAP) Pensacola beach* (pp. 107–117). Springer. https://doi.org/10.1007/978-94-017-0299-7_11

Tymofyeyeva, E., & Fialko, Y. (2015). *Solid Earth Mitigation of atmospheric phase delays in InSAR data, with application to the eastern California shear zone*. Abstract. https://doi.org/10.1002/2015JB011886

Wdowinski, S., Kim, S.-W., Amelung, F., & Dixon, T. H. (2006). *Wetland InSAR: A new space-based hydrological monitoring tool of wetlands surface water level changes* (Vol. 1). European Space Agency, (Special Publication) ESA SP.

Wegmüller, U., Walter, D., Spreckels, V., & Werner, C. L. (2010). Nonuniform ground motion monitoring with TerraSAR-X persistent scatterer interferometry. *IEEE Transactions on Geoscience and Remote Sensing*, *48*(2), 895–904. https://doi.org/10.1109/TGRS.2009.2030792

Williams, S., Bock, Y., & Fang, P. (1998). Integrated satellite interferometry: Tropospheric noise, GPS estimates and implications for interferometric synthetic aperture radar products. *Journal of Geophysical Research*, *103*(B11), 27051–27067. https://doi.org/10.1029/98jb02794

Yao, Y., Xu, C., Shi, J., Cao, N., Zhang, B., & Yang, J. (2015). ITG: A new global GNSS tropospheric correction model. *Scientific Reports*, *5*(1), 10273. https://doi.org/10.1038/srep10273

Yu, C., Li, Z., Penna, N. T., & Crippa, P. (2018). Generic atmospheric correction model for interferometric synthetic aperture radar observations. *Journal of Geophysical Research: Solid Earth*, *123*(10), 9202–9222. https://doi.org/10.1029/2017JB015305

Zebker, H. (2021). Accuracy of a model-free algorithm for temporal InSAR tropospheric correction. *Remote Sensing*, *13*(3), 1–9. https://doi.org/10.3390/rs13030409

Zebker, H. A., Rosen, P. A., & Hensley, S. (1997). Atmospheric effects in interferometric synthetic aperture radar surface deformation and topographic maps. *Journal of Geophysical Research*, *102*(10), 7547–7563. https://doi.org/10.1029/96JB03804

Zebker, M. S., Chen, J., & Hesse, M. A. (2023). Robust surface deformation and tropospheric noise characterization from common-reference interferogram subsets. *IEEE Transactions on Geoscience and Remote Sensing*, *61*, 1–14. https://doi.org/10.1109/TGRS.2023.3288019